

See discussions, stats, and author profiles for this publication at: <https://www.researchgate.net/publication/260159179>

# Chemical Vapor Synthesis and Structural Characterization of Nanocrystalline Zn<sub>1-x</sub>CoxO ( $x=0-0.50$ ) Particles by X-ray Diffraction and X-ray Absorption Spectroscopy

ARTICLE *in* THE JOURNAL OF PHYSICAL CHEMISTRY C · MAY 2010

Impact Factor: 4.77 · DOI: 10.1021/jp908148y

---

CITATIONS

18

READS

27

## 4 AUTHORS, INCLUDING:



Ruzica Djenadic

Technical University Darmstadt / Helmholtz-Zentrum für Materialien und Energie

16 PUBLICATIONS 81 CITATIONS

[SEE PROFILE](#)



Guvenc Akgul

Nigde Üniversitesi

15 PUBLICATIONS 68 CITATIONS

[SEE PROFILE](#)



Klaus Attenkofer

Brookhaven National Laboratory

80 PUBLICATIONS 792 CITATIONS

[SEE PROFILE](#)

# Chemical Vapor Synthesis and Structural Characterization of Nanocrystalline $Zn_{1-x}Co_xO$ ( $x = 0\text{--}0.50$ ) Particles by X-ray Diffraction and X-ray Absorption Spectroscopy

Ruzica Djenadic,<sup>†</sup> Güvenç Akgül,<sup>‡,§</sup> Klaus Attenkofer,<sup>‡</sup> and Markus Winterer\*,<sup>†</sup>

*Nanoparticle Process Technology, Faculty of Engineering, and Center for NanoIntegration Duisburg-Essen, CeNIDE, University of Duisburg-Essen, Germany, Advanced Photon Source, Argonne National Laboratory, 9700 South Cass Avenue, Argonne, Illinois 60439, and Physics Department, University of Cukurova, 01330 Adana, Turkey*

Received: August 24, 2009; Revised Manuscript Received: March 25, 2010

Nanocrystalline  $Zn_{1-x}Co_xO$  ( $x = 0\text{--}0.50$ ) particles are produced by chemical vapor synthesis using laser flash evaporation as a novel precursor delivery method. The crystal and local structure of the samples is studied using X-ray diffraction and X-ray absorption spectroscopy. A single wurtzite phase is observed in samples with cobalt contents as high as  $x = 0.25$  (actual content is 0.33 determined by atomic absorption spectroscopy). X-ray absorption spectra show that the  $Co^{2+}$  ions are incorporated into the  $ZnO$  wurtzite lattice substituting  $Zn^{2+}$  ions for cobalt contents between  $x = 0.001$  and  $x = 0.20$ . Only small lattice deformations are observed in these solid solutions.

## 1. Introduction

Initiated by theoretical predictions,<sup>1,2</sup> diluted magnetic semiconductors (DMSs) or semimagnetic semiconductors (SMSCs) have attracted increasing attention as potential candidates for spintronic devices. The key requirement for practical applications is the generation of intrinsic ferromagnetism with Curie temperatures above room temperature. Many studies on  $ZnO$  doped with cobalt<sup>3–5</sup> or other transition metal (TM) elements<sup>6–8</sup> have recently been reported. Due to the short-range nature of the ferromagnetic coupling, a heavy incorporation of TM atoms is required to stabilize the ferromagnetic state.<sup>9</sup> However, a major challenge for the preparation of DMS is the precipitation of second phases or clusters which may mask ferromagnetism due to intrinsic carrier mediated spin polarization. The source for these problems is the limited solubility of the dopants in  $ZnO$  which are in a thermodynamically metastable state. Therefore, nonequilibrium techniques are preferable to achieve higher doping concentrations.<sup>10</sup>

Previously, we have studied chromium-doped  $ZnO$ <sup>6,11</sup> and found only partial substitution of zinc by chromium. Divalent cobalt seems to be a good candidate for substitutional doping in  $ZnO$  which is one requirement for intrinsic carrier mediated spin polarization, since stable divalent cobalt and zinc oxides exist, the ionic radii of the cations are very similar, and tetrahedral coordination is also commonly observed. The nonequilibrium technique chemical vapor synthesis (CVS)<sup>12</sup> is used employing laser flash evaporation as a novel precursor delivery method to generate the  $Zn_{1-x}Co_xO$  nanoparticles. This method allows the generation of complex oxides from precursors of low volatility.<sup>13</sup> For a better insight into the effect of doping of  $ZnO$  on its crystal structure and magnetic properties, both long-range ordering and local structure should be analyzed in detail. Most reported experiments include only the crystal structure<sup>14–16</sup> or local structure<sup>10,17–20</sup> of Co-doped  $ZnO$ . The

detailed structural characterization of the Co-doped  $ZnO$  nanoparticles presented in this paper eliminate clustering and second phase formation as a possible source of the magnetic behavior. Rietveld refinement<sup>21</sup> of X-ray data was used to study the crystal structure. Extended X-ray absorption fine structure (EXAFS) and X-ray absorption near-edge structure (XANES) spectra are analyzed in detail in order to investigate the local structure around Co and Zn and their distribution in the  $Zn_{1-x}Co_xO$  nanoparticles.

## 2. Experimental Methods

**Powder Synthesis.** Nanocrystalline zinc oxide particles doped with cobalt ( $Zn_{1-x}Co_xO$ ) are produced by CVS with Co contents between  $x = 0$  and  $x = 0.50$ . The experimental setup is illustrated in Figure 1. Anhydrous solid zinc acetate,  $Zn(OAc)_2$  (Sigma Aldrich, 99.9% purity), and cobalt acetate,  $Co(OAc)_2$  (Sigma Aldrich, 99.9% purity), powders are thoroughly mixed corresponding to a nominal Co content  $x$ . The powders were mixed in a mortar inside a glovebox and then transferred under inert conditions to the laser flash evaporator. The radiation (50 W) of a  $CO_2$  laser (Coherent GEM 100 W) is used to evaporate the precursor mixture.<sup>13</sup> The precursor vapors are transported into the hot wall reactor using helium (1020 sccm) as carrier gas. The reactor consists of two sequential furnaces, where the precursors react with oxygen (1000 sccm) and form oxide particles. A hot wall temperature of 1100 °C and a total pressure of 20 mbar were used. The particles are thermophoretically separated from the gas flow in a particle collector.

**Chemical Analysis.** Atomic absorption spectroscopy (AAS) has been used to determine the actual cobalt content  $x_a$  in the as-synthesized particles. The measurement was carried out using a Thermo Scientific Atomic Absorption Spectrometer (M Series).

**Structural Characterization.** The crystal structure and phase composition of the as-synthesized samples are determined by X-ray diffraction (XRD) using a PANalytical X-ray diffractometer (X'Pert PRO) with Ni-filtered  $Cu K\alpha$  (1.5406 Å) radiation produced at 40 kV and 40 mA. The data are recorded over the  $2\theta$  range from 20 to 120° with a step size of 0.03° and a

\* Corresponding author. E-mail: markus.winterer@uni-due.de. Phone: +49-203-379-4446. Fax: +49-203-379-4453.

<sup>†</sup> University of Duisburg-Essen.

<sup>‡</sup> Argonne National Laboratory.

<sup>§</sup> University of Cukurova.

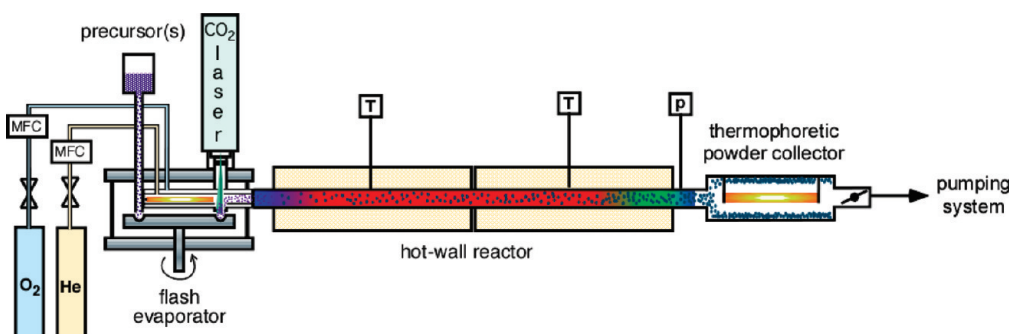


**Figure 1.** CVS reactor for the preparation of Co-doped ZnO with laser flash evaporator, hot wall reactor, and thermophoretic powder collector as modules.

sampling time of 200 s/step using an X'Celetor detector. Detailed structural analyses are performed by Rietveld refinement of the X-ray data using the MAUD program.<sup>22</sup> Results reported by Kihara et al. for ZnO<sup>23</sup> and data reported by Liu et al. and Wyckoff for CoO and Co<sub>3</sub>O<sub>4</sub>, respectively,<sup>24,25</sup> are used as initial structural parameters for the refinements. The Rietveld analysis provides information about phase composition, lattice parameters ( $a, b$ ), atomic position parameters ( $u$ ), and microstructural parameters (microstrain and crystallite size (coherent diffracting domain size,  $d$ )).

In order to investigate the local structure of the Co in Co-doped ZnO nanoparticles, X-ray absorption spectra are measured at the Co *K*-edge and Zn *K*-edge using beamline 12.BM.B at the Advanced Photon Source (APS). The beamline 12.BM.B is a bending magnet beamline dedicated to spectroscopy and scattering experiments and has an energy range of 7.5–28 keV. The absorption of the samples is optimized by diluting appropriate amounts of sample homogeneously into starch powder and pressing a pellet uniaxially. Transmission and fluorescence spectra are collected at ambient temperature. The spectra of commercial CoO and Co<sub>3</sub>O<sub>4</sub> powders (Sigma Aldrich) are also recorded as a reference.

Two different methods were applied to analyze the XAFS data. In the first approach, the program *xafsX*<sup>26</sup> is used for XAFS data reduction. The extracted EXAFS data are then analyzed by the Reverse Monte Carlo Method (RMC) using the *rmcxas* program.<sup>27</sup> Both, unfiltered and filtered (by Fourier back transformation from *R*-space between 0.5 and 3.5 Å) data are investigated. The structural results—pair distribution functions and their moment analysis—are within statistical error identical; however, the RMC analysis of filtered data is converging better, since most multiple scattering signals are eliminated. Multiple scattering would only be possible to fit using higher order correlation functions. Therefore, we describe only the results for the filtered data. Initial atom configurations are generated from results of the Rietveld refinements of X-ray diffraction data of the corresponding samples and contain an appropriate number of Co atoms. Zn- and Co-EXAFS spectra are analyzed simultaneously using a single atomic configuration where an appropriate number of Zn atoms are substitutionally replaced in a wurtzite lattice by Co atoms. Theoretical amplitude and phase functions for RMC analysis are obtained by FEFF 8 simulations.<sup>28</sup>

In the second approach, *ATHENA* and *ARTEMIS* programs<sup>29</sup> were used to analyze the XAFS data. *ATHENA* and *ARTEMIS* use the programmer's interface to IFEFFIT.<sup>30</sup> *ATHENA* is used for data processing (spectra normalization and background subtraction by the *AUTOBK* algorithm). *ARTEMIS* takes the experimental  $\chi(k)$  data and compares it with a theoretical function that is built up using the theoretical EXAFS paths

previously calculated with FEFF 8.2. The FEFF input files were created using *ATOMS*<sup>31</sup> and ZnO crystallographic data built in *ARTEMIS*. The EXAFS data are also analyzed using *ARTEMIS* and FEFF 8.2 programs. *ARTEMIS* is a program for analyzing

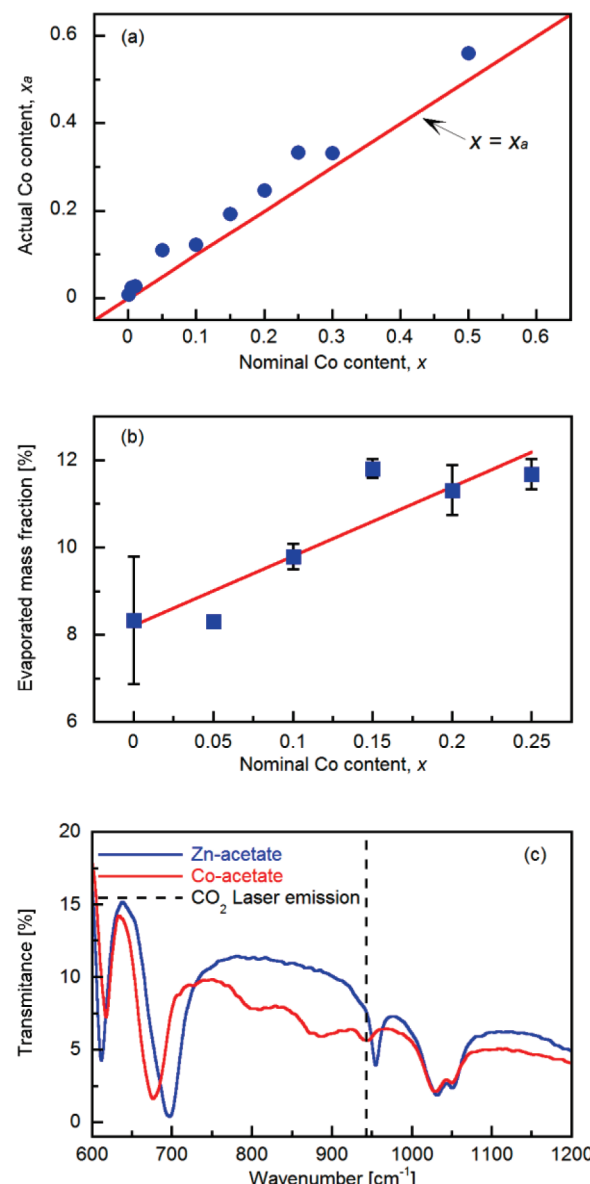


**Figure 2.** Correlation between actual,  $x_a$ , and nominal,  $x$ , Co content (a), precursor evaporation rate as a function of Co content (b), and comparison of FTIR spectra of the two precursor materials and the emission line of the CO<sub>2</sub> laser (wavelength of 10.6 μm) (c).

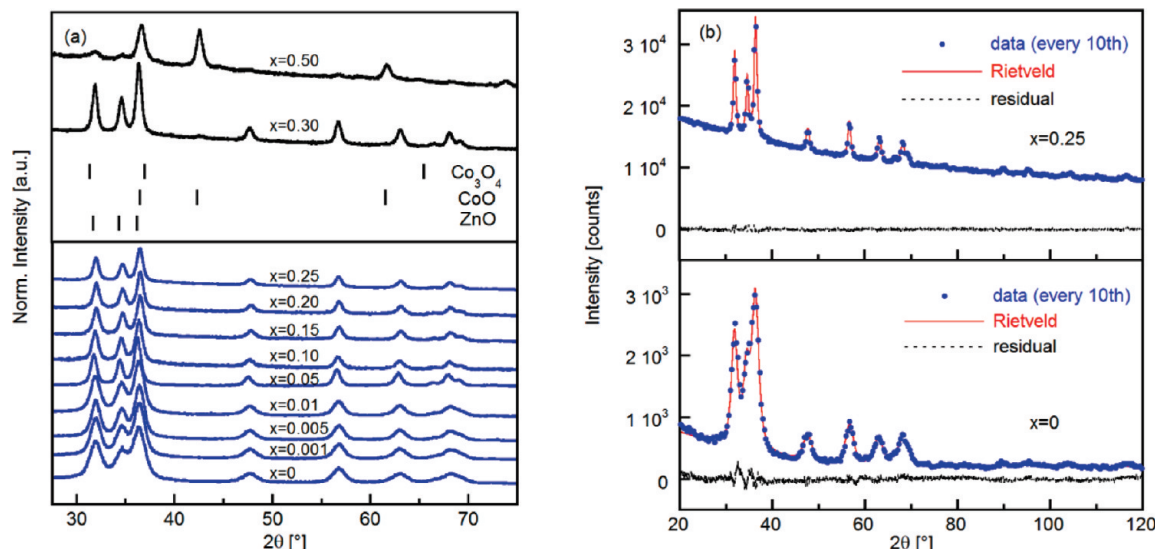


**Figure 3.** XRD patterns (a) of as-synthesized  $Zn_{1-x}Co_xO$  nanoparticles (vertical bars correspond to the three most pronounced Bragg reflections for wurtzite  $ZnO$ ,  $CoO$ , and  $Co_3O_4$ ) and Rietveld refinements (b) of the patterns for samples with Co content of  $x = 0$  and  $x = 0.25$ .

EXAFS data and uses  $\chi(k)$  as its input. FEFF 8.2 is used as an external program to calculate basic spectra for XANES fitting. ARTEMIS works within the framework of FEFF's multiple-scattering path expansion,<sup>32,33</sup> which means that the data are described as a summation of one or more scattering paths as computed by FEFF. FEFF 8.2 is a self-consistent real space multiple-scattering code for simultaneous calculations of X-ray absorption spectra and electronic structure. The output includes extended X-ray absorption fine structure (EXAFS), full multiple scattering calculations of various X-ray absorption spectra (XAS), and projected local densities of states (LDOS).

The results of both approaches which are methodologically and numerically completely different are compared in the following section.

### 3. Results and Discussion

**Chemical Analysis and X-ray Diffraction.** The chemical analysis by AAS (Figure 2a) shows that the actual Co concentration ( $x_a$ ) in the synthesized nanoparticles is systematically higher compared to the nominal concentration ( $x$ ) of the precursor mixture used. It is also observed that the evaporation rate of the precursor mixture as determined from its mass loss is enhanced with increasing Co concentration (Figure 2b) which may explain the systematic deviation of the actual and the nominal Co concentration. The evaporation rate is increasing with Co content because the Co acetate absorbs more light compared to the Zn acetate precursor at the wavenumber corresponding to the narrow  $CO_2$  laser emission (Figure 2c).

In Figure 3a, XRD patterns of as-synthesized  $Zn_{1-x}Co_xO$  nanoparticles are presented. The substitution of Co did not cause remarkable changes in the diffraction patterns for Co contents up to  $x \leq 0.25$ . Rietveld refinement of XRD data shows that those particles are of wurtzite structure, while in particles with Co concentration  $x \geq 0.30$   $CoO$  and  $Co_3O_4$  are present as additional phases (Figure 3b). The maximum cobalt solubility in wurtzite type  $ZnO$ , for which the particles are still single-phase, varies greatly for samples of the same nominal composition but prepared by different methods.<sup>7,14,15,34,35</sup> Recently, Straumal et al. found that the solubility of Co and Mn increases with decreasing grain size.<sup>36,37</sup> They show that the solubility increases with decreasing grain size with Co in  $ZnO$  from 2 at. % in the bulk and up to about 40 at. % in

polycrystalline samples with grain sizes below 20 nm. The Co solubility limit in our particles is about  $x_a = 0.33$  ( $x = 0.25$ ) (see Figure 3a). The crystallite size, extracted using the Rietveld refinement of the XRD data, ranges from about 9 nm for undoped samples (Figure 4a) up to 20 nm for the sample with a Co content of  $x = 0.25$ . Further Co addition causes the generation of second phases:  $CoO$  in the sample with a nominal Co content of  $x = 0.30$  ( $x_a = 0.332$ ) and  $CoO$  and  $Co_3O_4$  in the sample with  $x = 0.50$  ( $x_a = 0.56$ ). This is consistent with the finding of Straumal et al.<sup>36</sup>

The incorporation of Co ions into the wurtzite structure leads not only to an increase of crystallite size (coherent diffracting domain size  $d$ ) but also to a decrease of the microstrain, Figure 4b. The observation of an increase of crystallite size with increasing dopant content is opposite to other doping elements such as chromium or aluminum<sup>6,38</sup> where impurity drag is slowing down particle growth by coalescence. The origin for this observation is likely due to the increased evaporation rate with increasing Co content in the precursor mixture (Figure 2b). A fit with the growth law for monodisperse particles by coagulation<sup>39</sup> where  $d_0$  is the initial particle diameter,  $N_0$  is the initial number concentration (which is assumed to increase linearly with the Co precursor concentration), and  $\beta$  is the coagulation coefficient

$$d = d_0(1 + N_0\beta t)^{1/3} \quad (1)$$

agrees with the experimental data in Figure 4a. Therefore, the cause for the decrease in microstrain is not because of the introduction of Co into the wurtzite lattice as Figure 4b might suggest, but it is due to the decrease of surface to volume ratio with increase of crystallite size as it correlates linearly (Figure 4c) with the relative number of atoms at the particle surface to the particle volume which is estimated by

$$\frac{N_{\text{surface}}}{N_{\text{volume}}} \approx 1 - \left(1 - \frac{c}{r}\right)^3 \quad (2)$$

where the lattice constant  $c$  is used to estimate the relaxation length ('surface thickness') and  $r$  is the radius of a sphere

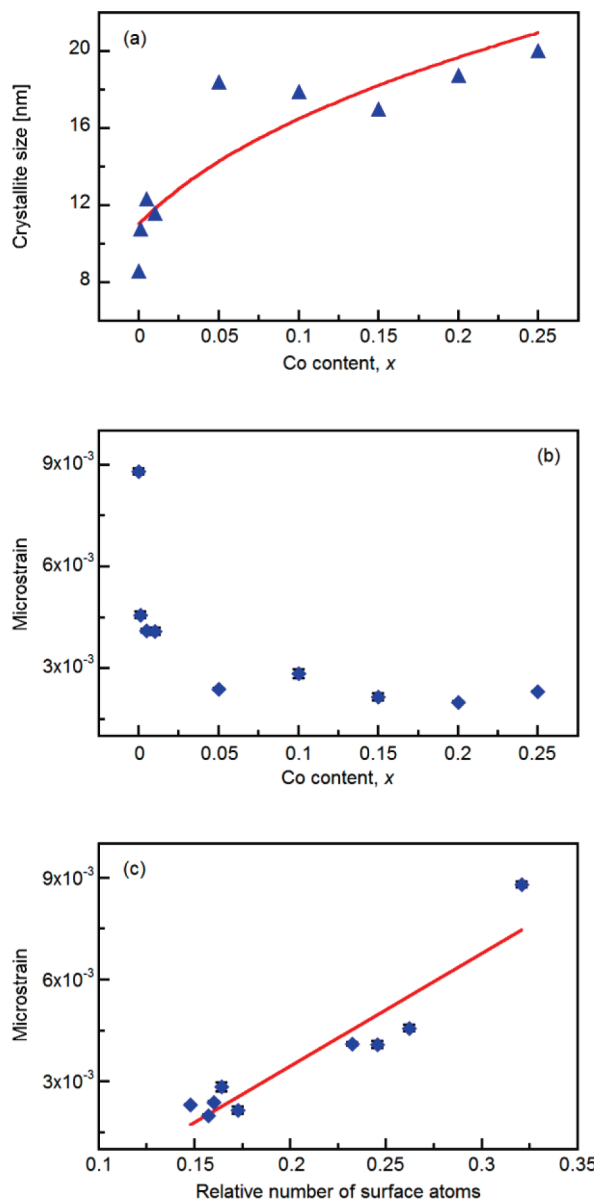


**Figure 4.** Crystallite size fit (a) according to monodisperse coagulation (eq 1) and microstrain as a function of actual Co content (b) in  $Zn_{1-x}Co_xO$  samples and as a function of the relative number of atoms on the particle surface (eq 2) (c).

equivalent in volume to the average particle. Since the valence of Co and Zn in Co-doped ZnO is identical and the ionic radius for both is similar, the microstrain is varying little above Co contents of  $x = 0.05$ .

Up to  $x_{Co} = 0.25$ , the X-ray diffractograms could be refined using a single wurtzite phase (Figure 3). The lattice parameters of  $Zn_{1-x}Co_xO$  wurtzite obtained from Rietveld refinements are presented in Figure 5. It is found that Co substitution causes an elongation along the  $a$ -axis, while no significant change for the  $c$ -axis is observed. As a result, the unit cell volume increases and the  $c/a$  ratio decreases (Figure 6). A similar behavior is reported by Kolesnik et al.<sup>7</sup> Considering that the ionic radius of tetrahedrally coordinated  $Co^{2+}$  ( $0.58 \text{ \AA}$ ) is only slightly smaller than  $Zn^{2+}$  ( $0.60 \text{ \AA}$ ),<sup>40</sup> no changes in  $c$ - or  $a$ -direction are expected. Jin et al. report similar observations concerning the  $c$ -axis in Co-doped films.<sup>41</sup> The elongation along the  $a$ -axis up to  $x = 0.005$  is therefore possibly the result of lattice relaxation.<sup>42,43</sup> The surface to volume ratio decreases as the size of crystallites increases. This leads to a reduction of the relative

number of surface atoms and consequently to lattice relaxation. Therefore, a linear correlation with the relative number of surface atoms is observed (Figure 5b). Since the surface energies of ZnO are anisotropic ( $ZnO$  (0001)  $1.7 \text{ J/m}^2$ ,  $ZnO$  (1100)  $0.9 \text{ J/m}^2$ ),<sup>44</sup> it can be expected that this effect varies with crystallographic orientation. This may be the origin of the different trend for lattice constants  $a$  and  $c$ . Above  $x = 0.25$ , a rocksalt and mixture of rocksalt and phases are observed (Figure 3). For  $x = 0.25$  (Figure 6a), the  $c/a$  ratio is decreasing below 1.6. The transition from wurtzite to rocksalt has been observed with increasing pressure at 9 GPa in the case of pure ZnO<sup>45</sup> for  $c/a < 1.6$ . However, with increasing pressure, the unit cell volume decreases which is opposite from our observation (Figure 5a). The oxygen positional parameter in  $c$ -direction,  $u$ , describes the relative position of the anion to the cation sublattice in wurtzite,<sup>46</sup> and  $u^*c/a$  for an ideal wurtzite lattice would be  $(3/8)^{1/2}$ ,<sup>46</sup> which is observed for our pure ZnO nanocrystals and is close to the bulk value (Figure 6a).

Zhang et al.<sup>47,48</sup> investigated Co-doped ZnO prepared by conventional solid state reaction of pellets of mixed ZnO and Co metal powders sintered at 1473 K for 10 h. The fraction of aggregated Co ions as determined by fitting magnetic susceptibility data is higher than expected for a statistical, homogeneous distribution of Co ions. Corresponding DFT calculations<sup>47</sup> suggest that Co dopants have a tendency to cluster along the  $ab$  plane. According to X-ray diffraction,<sup>48</sup> the lattice constant  $c$  is decreasing with increasing Co content, different from our observations. The preparation method by Zhang et al. starts with a highly inhomogeneous mixture treated for a very long time at elevated temperatures. CVS is a nonequilibrium process where gaseous precursors are mixed on the molecular level. Therefore, differences in the incorporation of dopant atoms are inevitable. Toulemonde and Gaudon<sup>49</sup> performed an analysis of their magnetic susceptibility data similar to Zhang et al.<sup>47</sup> and found that Co is homogeneously distributed in ZnO between 0.5 and 10% for samples prepared by the Pechini method including a heat treatment at 1273 K for 10 h. Small deviations of the fraction of Co–Co dimers from the binomial distribution are interpreted as a nonperfectly randomized distribution or slight segregation. The results of Zhang et al.<sup>47</sup> follow the same binomial distribution. From these contradictory interpretations of similar Co–(O)–Co dimer formation probabilities, it seems at present difficult to derive a final conclusion concerning the state of dispersion of Co in ZnO from magnetic susceptibility data alone.

Li et al.<sup>50</sup> investigated Co-doped ZnO nanocrystals prepared by a sol–gel method using DMSO as solvent, stirring the reaction mixture for 12 h and annealing at 673 K for 1 h. They interpret their XRD results together with Raman and UV/vis spectra by a surface segregation due to self-purification above  $x = 0.05$  in  $Zn_{1-x}Co_xO$  where the lattice constant  $a$  and the unit cell volume increase and  $c$  decreases (slightly) with increasing Co content. For  $x = 0.2$ , a second  $Co_3O_4$  phase is observed. In our samples, second phase formation is only observed above  $x = 0.25$  ( $x_a = 0.33$ ), the variations of the lattice constants correlate with the number of surface atoms (Figure 5), and the detailed EXAFS data analysis (see below) does not provide indications for phase separation on the local level. Therefore, we conclude that the observed increase in the lattice constant  $a$  by  $0.005 \text{ \AA}$  for samples from  $x = 0.1$  to  $0.25$  cannot be used to suggest surface segregation by self-purification.

**X-ray Absorption Fine Structure.** Element specific X-ray absorption spectroscopy provides information about the distribution and location of Co in the wurtzite lattice complementary

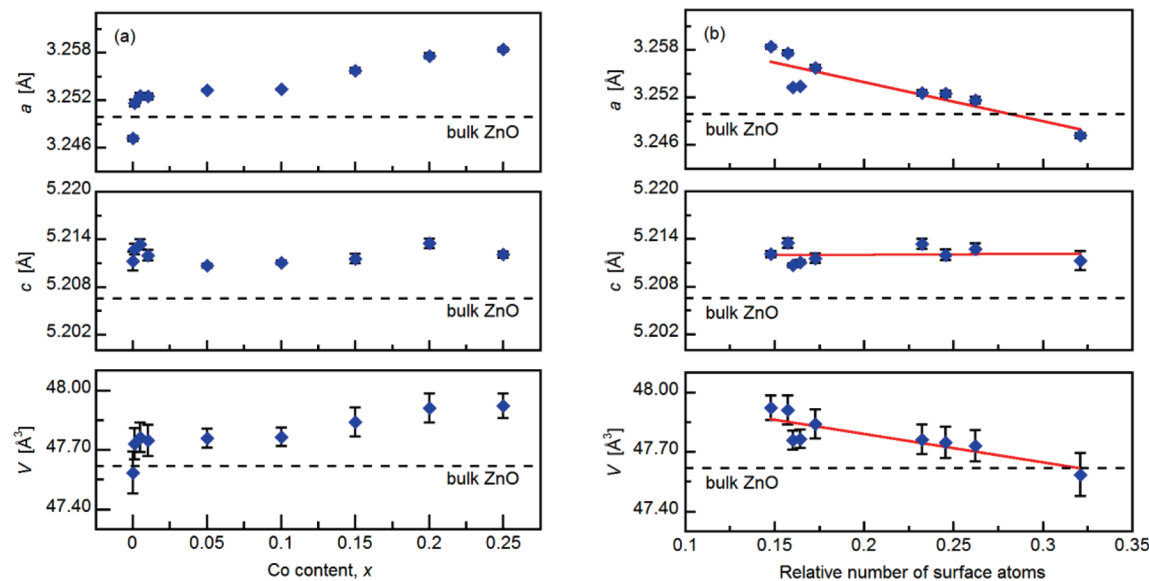


**Figure 5.** Lattice parameters  $a$  and  $c$  and unit cell volume of the  $Zn_{1-x}Co_xO$  samples (bulk values for ZnO are literature data) as a function of Co content (a) and relative number of surface atoms (b).

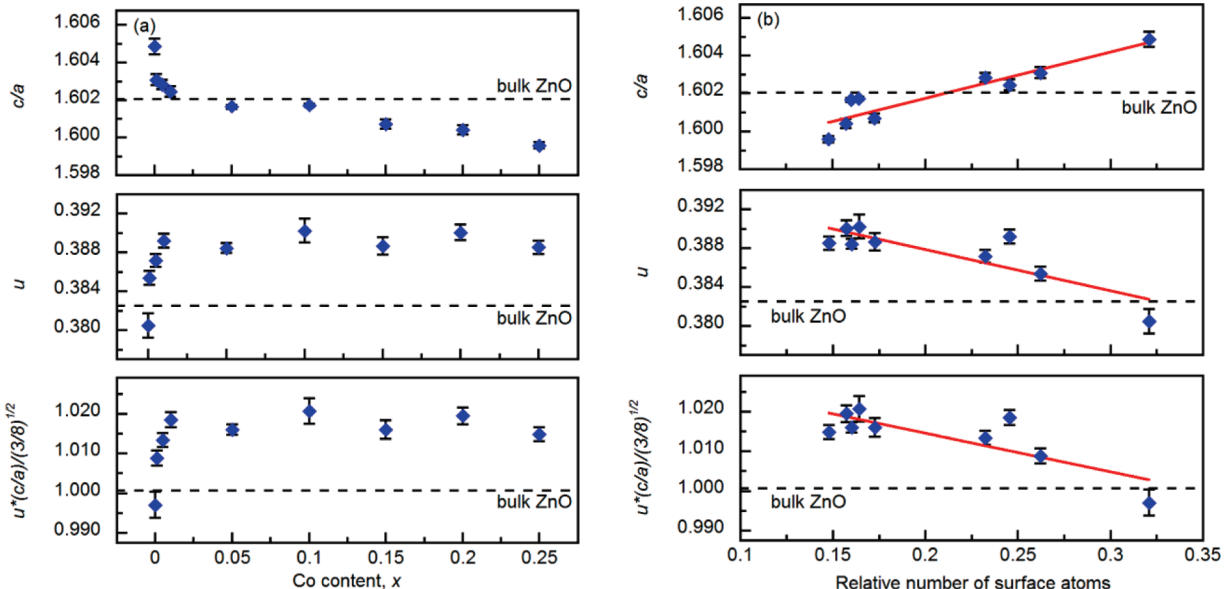


**Figure 6.** Structural parameters determined from Rietveld refinement as a function of Co content (a) and as a function of relative number of surface atoms (b).

to X-ray diffraction which is not sensitive to segregation or the formation of very small precipitates of second phases especially at low dopant concentration. Therefore, samples for which XRD data showed only a single wurtzite phase,  $x < 0.25$ , have also been studied by XAFS. Figure 7 shows normalized Co and Zn  $K$ -edge XANES spectra of the  $Zn_{1-x}Co_xO$  together with reference spectra of Co metal, CoO, and  $Co_3O_4$ , and theoretical XANES spectra for Co-doped ZnO. Full multiple scattering simulations using FEFF 8.2 are used to compute theoretical XANES spectra. Comparing the XANES spectra of  $Zn_{1-x}Co_xO$  with the spectra of the CoO reference reveals that the Co is present in the  $Co^{2+}$  valence state. The existence of Co metal and cobalt oxides can be excluded using fingerprint methods due to the different spectral features of  $Zn_{1-x}Co_xO$  as compared with that of cobalt oxides. The small pre-edge peak at about 7708 eV appears due to the transition of Co 1s electron to 4p–3d hybridized states in tetrahedral symmetry.<sup>19</sup> The shoulder above

the absorption edge in the Zn  $K$ -edge XANES spectra at 9680 eV (Figure 7b) is related to scattering contributions from high coordination shells.<sup>10</sup> The FEFF simulations of XANES spectra for Co replacing Zn substitutionally in the wurtzite lattice are in qualitative agreement with the experimental spectra.

The Co  $K$ -edge EXAFS for  $Zn_{1-x}Co_xO$ , and the Zn  $K$ -edge for ZnO powder, as well as their Fourier transforms are shown in Figure 8a and b, respectively, and the Zn  $K$ -edge EXAFS for  $Zn_{1-x}Co_xO$ , and the Zn  $K$ -edge for ZnO powder, as well as their Fourier transforms are shown in Figure 8c and d, respectively. From Figure 8a, it can be seen that the spectra as well as the amplitude of the Fourier transforms for  $Zn_{1-x}Co_xO$  are very close to that of pure ZnO, indicating that Co is replacing Zn substitutionally. From the radial structure functions (no phase shift correction applied) of ZnO and  $Zn_{1-x}Co_xO$  (Figure 8b), three peaks can be observed. The first peak at about 1.6 Å is due to the Co–O coordination in the first shell, the second peak

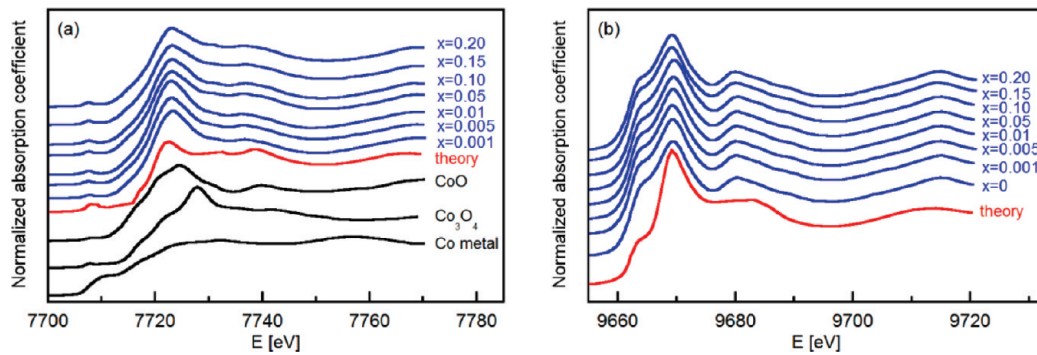


**Figure 7.** Co *K*-edge XANES spectra of  $Zn_{1-x}Co_xO$ , CoO,  $Co_3O_4$ , and Co metal and theoretical calculation for Co-doped ZnO (a) and Zn *K*-edge XANES spectra for  $Zn_{1-x}Co_xO$  and theoretical calculation for Co-doped ZnO (b).

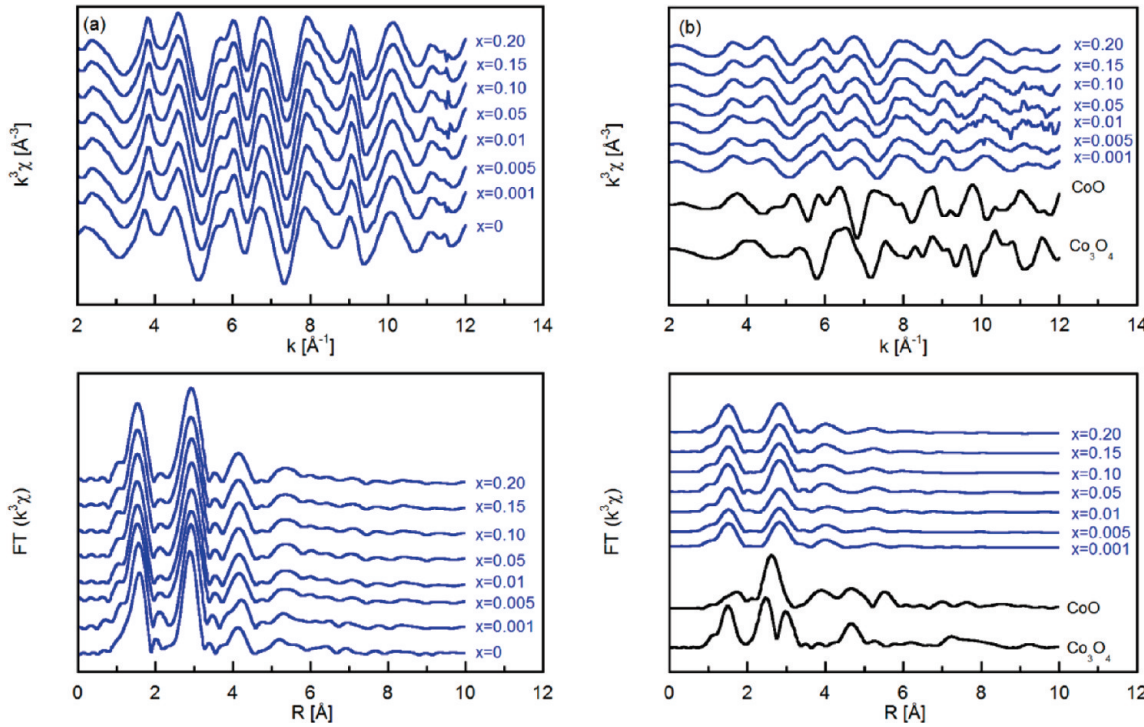


**Figure 8.** EXAFS spectra (top) and radial structure functions (bottom) on Zn *K*-edge (a) and Co *K*-edge (b) for  $Zn_{1-x}Co_xO$ .

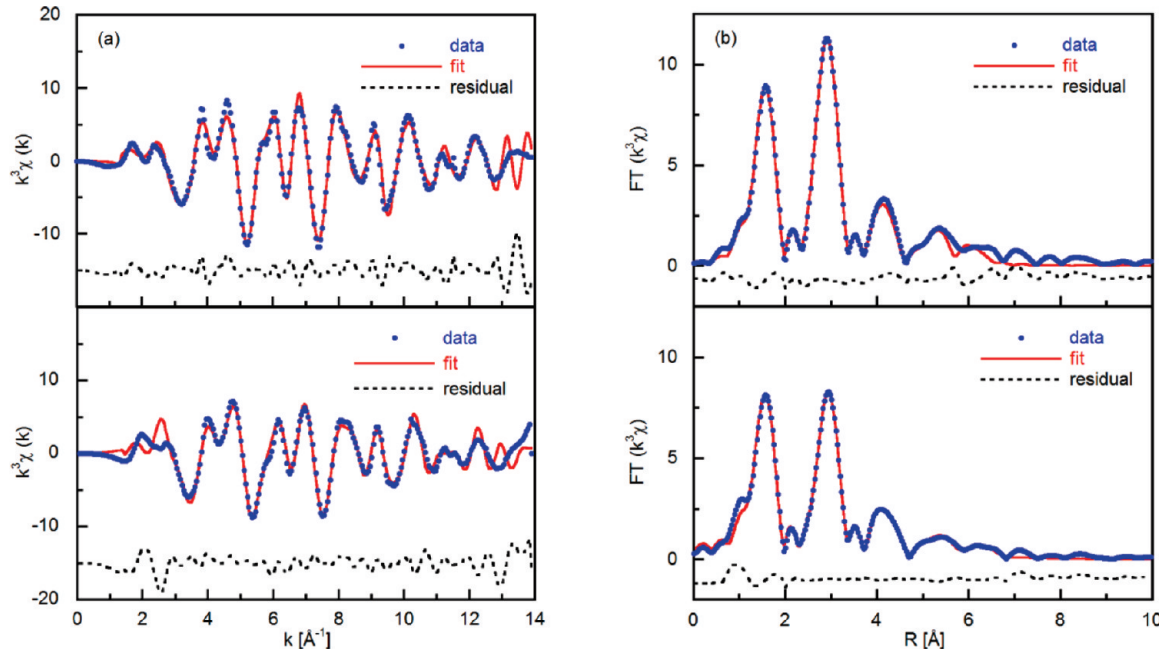


**Figure 9.** ARTEMIS fit of the Zn (top) and Co *K*-edge EXAFS spectra (bottom) of  $Zn_{0.85}Co_{0.15}O$  (a) and corresponding radial structure functions (b).

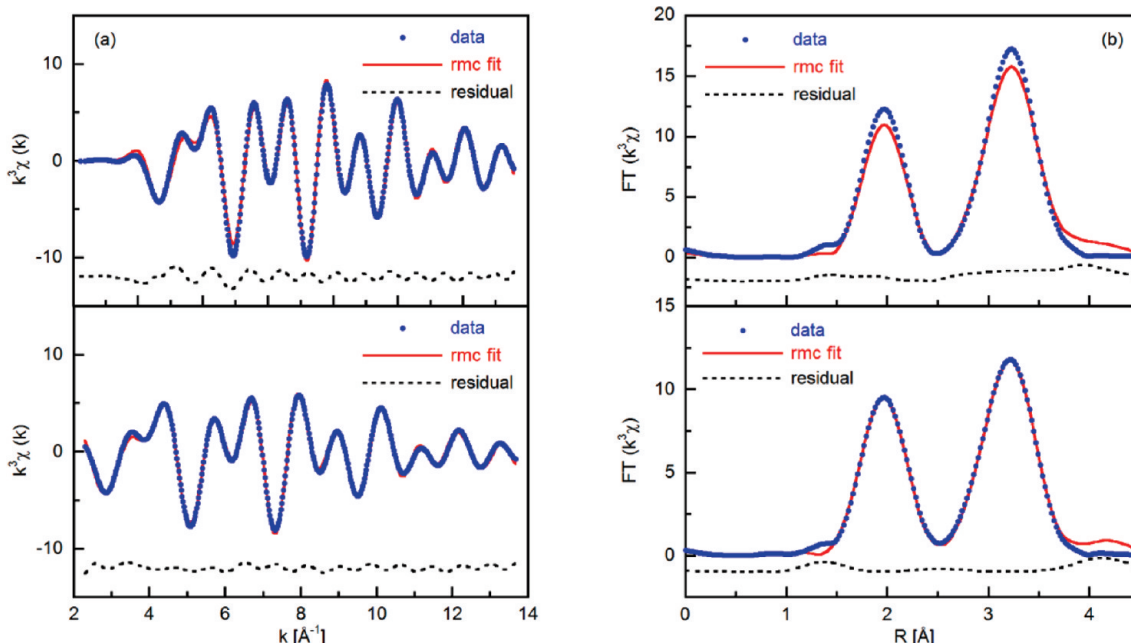


**Figure 10.** RMC analysis of EXAFS spectra of  $Zn_{0.80}Co_{0.20}O$  using a single, mutual model for Zn  $K$ -edge (top) and Co  $K$ -edge spectra (bottom) (a) and their phase corrected radial structure functions (b).

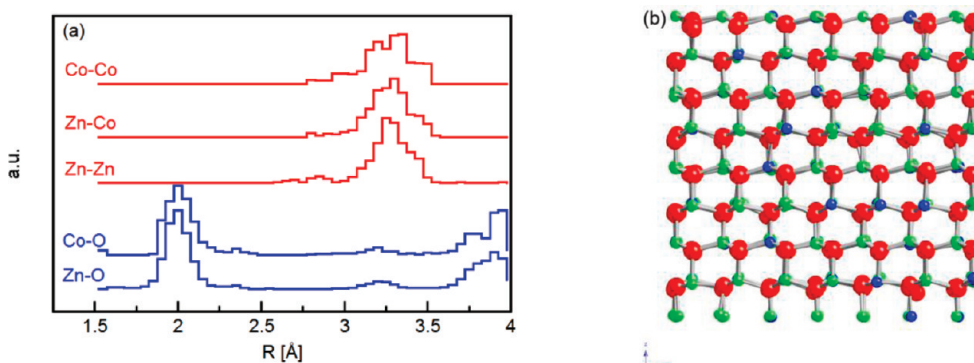


**Figure 11.** Partial pair distribution functions for  $Zn_{0.80}Co_{0.20}O$  derived from RMC analysis of EXAFS data (a) and the corresponding atomic configuration (b) (Zn, green; Co, blue; O, red spheres).

at about 2.5 Å corresponds to the Zn(Co)–Zn coordination in the second shell, and the third at about 4 Å arises from the third coordination shell comprised of nine oxygen atoms and multiple scattering. Positions and amplitudes of the first and second peaks do not change significantly with increasing Co content.

The data are fitted for all samples using ARTEMIS including multiple scattering<sup>32</sup> (see Figure 9 for  $Zn_{0.85}Co_{0.15}O$ , for example). The results are in good agreement with the experimental data up to about 6 Å. Data in the  $k = 3$ –12 Å<sup>-1</sup> range was Fourier transformed and fitted in real space in the  $R = 1$ –6.6 Å range for  $Zn_{1-x}Co_xO$  samples using a Hanning window function. Samples with  $x > 0.005$  are also analyzed using RMC (Figure 10) again in good agreement with the experimental data. Partial pair distribution functions derived from RMC analysis of the EXAFS spectra are shown in Figure 11 for  $Zn_{0.80}Co_{0.20}O$  as an example. The results of the ARTEMIS fits (interatomic distances, coordination numbers, and Debye–Waller factors) and the corresponding RMC analysis (moment analysis of the partial pair distribution functions up to the second moment) are compiled and compared in Table 1 for all doped samples as well as pure ZnO and bulk reference samples (CoO and  $Co_3O_4$ ).

The agreement between the two different, independent fitting approaches is excellent. Only the Debye–Waller factors obtained from the ARTEMIS fits are systematically smaller compared to the second moments determined from RMC partial pair distribution functions. Since ARTEMIS uses a Gaussian distribution function for the interatomic distances and RMC results for the second moment are determined from the numerically computed partial pair distribution functions, the deviation is likely to originate from the non-Gaussian shape of the distribution functions.

It can be seen from the results compiled in Table 1 that the interatomic distances of Co–O and Co–Zn in Co-doped ZnO samples are close to the Zn–O and Zn–Zn distances in pure ZnO in contrast to Liu et al.<sup>10</sup> who observed an elongation of Co–O distances and a contraction of Co–Zn distances and explained it by a mismatch of  $Co^{2+}$  in the ZnO lattice. The partial pair distribution functions (Figure 11) for Co–Co, Co–Zn, and Zn–Zn overlap and are not split. This is evidence that  $Co^{2+}$  ions occupy tetrahedral Zn sites substitutionally in the ZnO wurtzite lattice for doping levels  $x$  below 0.20. Figure 12 displays the interatomic distances as a function of Co content as determined from the RMC analysis together with the second

**TABLE 1: Results of EXAFS Data Analysis Using *rmcxas* and *ARTEMIS* for Co-Doped ZnO and Co Oxides**

method of analysis		RMC	ARTEMIS	RMC	ARTEMIS	RMC	ARTEMIS
$x$ (Co)	shell	$N$	$N$	$R$ ( $\text{\AA}$ )	$R$ ( $\text{\AA}$ )	$p_2$ ( $10^{-3} \text{ \AA}^2$ )	$\sigma^2$ ( $10^{-3} \text{ \AA}^2$ )
0 (ZnO)	Zn–O	3.6(7)	3.8(2)	1.96(2)	1.97(1)	7(2)	5.4(2)
	Zn–Zn	11(2)	11.4(2)	3.24(2)	3.22(1)	13(4)	11.3(1)
	Co–O	na <sup>a</sup>	4.3(1)	na	2.01(2)	na	9(1)
	Co–Zn		11.9(1)		3.22(2)		18(4)
	Co–Co		0.011(0)		3.21(0)		17(2)
	Zn–Co		0.011(2)		3.21(2)		9(1)
0.005	Zn–Zn		11.4(2)		3.23(2)		9(1)
	Co–O	na	4.27(1)	na	2.01(2)	na	10(2)
	Co–Zn		11.34(1)		3.22(2)		17(5)
	Co–Co		0.06(0)		3.21(0)		17(2)
	Zn–Co		0.06(0)		3.21(2)		11(2)
	Zn–Zn		11.9(1)		3.23(2)		11(3)
0.01	Co–O	3.9(6)	3.96(7)	2.02(2)	2.00(2)	10(3)	7(2)
	Co–Co	(0.06)	0.11(1)	(3.21) <sup>b</sup>	3.21(2)	na	18(4)
	Co–Zn	na	11.3(1)	na	3.21(0)	na	18(1)
	Zn–O	3.2(7)	na	1.95(2)	na	7(3)	Na
	Zn–Co	0.12(2)	0.114(1)	3.23(2)	3.21(2)	19(5)	14(3)
	Zn–Zn	9(2)	11.3(2)	3.25(3)	3.23(4)	12(4)	14(3)
0.05	Co–O	4.0(9)	3.7(5)	2.00(3)	1.97(4)	9(5)	6(2)
	Co–Co	0.38(8)	0.6(2)	(3.25(3))	2.94(3)	14(3)	4(15)
	Co–Zn	na	10.5(2)	na	3.20(4)	na	12(10)
	Zn–O	4.0(8)	3.8(1)	1.98(2)	1.97(1)	9(5)	6(1)
	Zn–Co	0.7(1)	0.57(2)	3.23(3)	3.20(2)	13(4)	8(3)
	Zn–Zn	11(3)	10.8(2)	3.24(3)	3.23(4)	12(5)	8(3)
0.10	Co–O	4.0(6)	3.8(5)	2.03(2)	1.98(3)	14(5)	7(2)
	Co–Co	1.1(2)	1.1(1)	3.25(2)	2.93(3)	10(3)	8(7)
	Co–Zn	na	10.4(2)	na	3.20(5)	na	13(7)
	Zn–O	3.8(7)	3.9(1)	1.98(2)	1.97(2)	12(6)	6(1)
	Zn–Co	1.5(3)	1.2(1)	3.23(2)	3.10(3)	18(4)	6(5)
	Zn–Zn	10(2)	10.7(3)	3.23(2)	3.24(2)	11(3)	10(2)
0.15	Co–O	4.0(8)	3.7(5)	2.01(3)	1.97(4)	12(6)	7(2)
	Co–Co	2.1(5)	1.7(2)	3.23(3)	2.95(2)	16(5)	12(10)
	Co–Zn		9.5(2)	na	3.20(10)	na	12(7)
	Zn–O	4.0(8)	3.4(2)	1.98(2)	1.97(1)	9(5)	4(5)
	Zn–Co	2.0(4)	1.8(2)	3.24(3)	3.20(2)	17(6)	5(7)
	Zn–Zn	10(2)	9.7(4)	3.22(3)	3.24(2)	19(9)	6(2)
0.20	Co–O	4.0(8)	3.73(5)	2.01(3)	1.97(4)	12(6)	6(2)
	Co–Co	2.6(5)	2.24(1)	3.22(3)	2.95(2)	24(8)	12(10)
	Co–Zn	na	8.9(3)	na	3.20(10)	na	14(10)
	Zn–O	4.0(8)	3.6(2)	1.98(2)	1.97(1)	9(5)	5(2)
	Zn–Co	2.6(6)	2.37(2)	3.24(3)	3.20(2)	19(8)	4(10)
	Zn–Zn	9(2)	9.5(4)	3.23(3)	3.25(3)	24(12)	10(3)
1.00 (CoO)	Co–O	5.8(8)	5.7(5)	2.10(3)	2.1(3)	46(10)	20(5)
	Co–Co	11(2)	11.4(3)	3.04(3)	3.02(3)	26(7)	13(7)
1.00 (Co <sub>3</sub> O <sub>4</sub> )	Co–O	5.0(8)	3.5(4)	1.96(2)	1.96(2)	20(8)	3.3(10)
	Co–Co	5(1)	10(2)	2.88(2)	3.4(2)	10(3)	10(3)

<sup>a</sup> Not analyzed. <sup>b</sup> The values in parentheses are only from one bin in the pair distribution function due to low Co content.

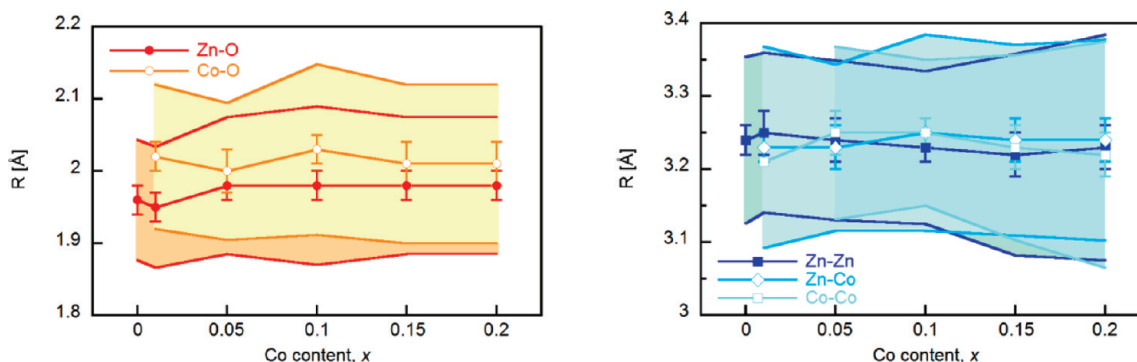


**Figure 12.** Nearest and next nearest interatomic distances according to RMC data analysis as a function of cobalt content as determined from moment analysis of the corresponding partial pair distribution functions (taken from Table 1). The shaded areas represent the square root of the second moment ( $R \pm p_2^{1/2}$  ( $\text{\AA}$ )).

moment. The Co–O distances deviate systematically to marginally larger distances compared to Zn–O distances, whereas the cationic distances overlap within the error bars. Both do not change as a function of Co content. Only the second moment

increases slightly at higher Co contents which could be an indication for an onset of the phase transformation to rocksalt structure at even higher Co contents or due to an increased static disorder.

#### 4. Conclusions

Data analysis of EXAFS spectra using *ARTEMIS* and *rmcxas* provides consistent and reliable structural information within the error limits. The advantage of *ARTEMIS* is the possible inclusion of multiple scattering and for *rmcxas* the use of an atomic configuration as a physical model to fit both Zn and Co spectra simultaneously. Clearly, it is difficult to determine the structural evolution of wurtzite type ZnO as a function of dopant content. Sample preparation procedures and conditions play a very important role in obtaining Co-doped ZnO samples of high homogeneity. CVS as a nonequilibrium process where precursors are mixed on the molecular level in the gas phase provides the possibility to prepare such samples.

A high solubility of cobalt in ZnO is achieved using chemical vapor synthesis, as Zn<sub>1-x</sub>Co<sub>x</sub>O nanoparticles for Co contents of up to  $x_a = 0.33$  (according to chemical analysis) are of single wurtzite phase. The crystallographic structure parameters vary continuously with increasing Co content due to the increasing crystallite size. The cause for the increase of crystallite size is the higher evaporation rate of the Co compared to the Zn precursor. Therefore, the observed subtle but significant variations of the structural parameters are due to the increasing surface to volume ratio with decreasing particle size. Detailed analysis of both crystallographic and local structure provides evidence that it is possible to prepare nanocrystalline ZnO particles by chemical vapor synthesis where Co is substituting Zn in the wurtzite lattice which is a key requirement for the development of dilute magnetic semiconductors based on Co-doped ZnO.

**Acknowledgment.** The financial support by the German Research Foundation (DFG) through the Collaborative Research Center SFB 445 is gratefully acknowledged. The authors thank Dr. Nadia Leyarovska from APS, Argonne National Laboratory, IL, for help at the EXAFS beamline and Andreas Gondorf and Prof. Dr. Axel Lorke, Experimental Physics, University of Duisburg-Essen, Germany, for FT-IR measurements.

#### References and Notes

- (1) Dietl, T.; Ohno, H.; Matsukura, F.; Cibert, J.; Ferrand, D. *Science* **2000**, *287*, 1019.
- (2) Sato, K.; Katayama-Yoshida, H. *Physica E* **2001**, *10*, 251.
- (3) Kim, Y.-I.; Page, K.; Seshadri, R. *Appl. Phys. Lett.* **2007**, *90*, 101904.
- (4) Bouloudene, M.; Viart, N.; Colis, S.; Kurtus, J.; Dinia, A. *Appl. Phys. Lett.* **2005**, *87*, 052501.
- (5) Chambers, S. A.; Droubay, T. C.; Wang, C. M.; Rosso, K. M.; Heald, S. M.; Schwartz, D. A.; Kittilstved, K. R.; Gamelin, D. R. *Mater. Today* **2006**, *9*, 28.
- (6) Jin, W.; Lee, I.-K.; Komph, A.; Dörfler, U.; Winterer, M. *J. Eur. Ceram. Soc.* **2007**, *27*, 4333.
- (7) Kolesnik, S.; Dabrowski, B.; Mais, J. *J. Appl. Phys.* **2004**, *95*, 2582.
- (8) Cong, C. J.; Hong, J. H.; Liu, Q. Y.; Liao, L.; Zhang, K. L. *Solid State Commun.* **2006**, *138*, 511.
- (9) Lee, E.-C.; Chang, K. *J. Phys. Rev. B* **2004**, *69*, 085205.
- (10) Liu, T.; Xu, H.; Chin, W. S.; Yong, Z.; Wee, A. T. S. *J. Phys. Chem. C* **2008**, *112*, 3489.
- (11) Schneider, L.; Zaitsev, S. V.; Jin, W.; Komph, A.; Winterer, M.; Acet, M.; Bacher, G. *Nanotechnology* **2009**, *20*, 135604.
- (12) Winterer, M., *Nanocrystalline Ceramics - Synthesis and Structure*; Springer Verlag: Berlin, 2002.
- (13) Winterer, M.; Srdic, V. V.; Djenic, R.; Komph, A.; Weirich, T. E. *Rev. Sci. Instrum.* **2007**, *78*, 123093.
- (14) Risbud, A. S.; Spaldin, N. A.; Chen, Z. Q.; Stemmer, S.; Seshadri, R. *Phys. Rev. B* **2003**, *68*, 205202.
- (15) Duan, L. B.; Chu, W. G.; Yu, J.; Wang, Y. C.; Zhang, L. N.; Liu, G. Y.; Liang, J. K.; Rao, G. H. *J. Magn. Magn. Mater.* **2008**, *320*, 1573.
- (16) Gaudon, M.; Toulemonde, O.; Demouragues, A. *Inorg. Chem.* **2007**, *46*, 10996.
- (17) Liu, X.-C.; Shi, E.-W.; Chen, Z.-Z.; Zhang, H.-W.; Song, L.-X.; Wang, H.; Yao, S.-D. *J. Cryst. Growth* **2006**, *296*, 135.
- (18) Shi, T.; Zhu, S.; Sun, Z.; Wei, S.; Liu, W. *Appl. Phys. Lett.* **2007**, *90*, 102108.
- (19) Sun, Z.; Yan, W.; Zhang, G.; Oyanagi, H.; Wu, Z.; Li, Q.; Wu, W.; Shi, T.; Pan, Z.; Xu, P.; Wei, S. *Phys. Rev. B* **2008**, *77*, 245208.
- (20) Han, A. R.; Hwang, S.-J.; Zhao, Y.; Kwon, Y.-U. *J. Magn. Magn. Mater.* **2008**, *320*, 1591.
- (21) Rietveld, H. M. *J. Appl. Crystallogr.* **1969**, *2*, 65.
- (22) Lutterotti, L.; Scardi, P. *J. Appl. Crystallogr.* **1990**, *23*, 246.
- (23) Kihara, K.; Donnay, G. *Can. Mineral.* **1985**, *23*, 647.
- (24) Liu, X.; Prewitt, C. T. *Phys. Chem. Miner.* **1990**, *17*, 168.
- (25) Wyckoff, R. W. G. *Crystal Structures*; John Wiley & Sons: New York, London, 1963; Vol. 1.
- (26) Winterer, M. *J. Phys. IV* **1997**, *7*, C2–243.
- (27) Winterer, M. *J. Appl. Phys.* **2000**, *88*, 5635.
- (28) Ankudinov, A. L.; Ravel, B.; Rehr, J. J.; Albers, R. C.; Conradson, S. D. *Phys. Rev. B* **1998**, *58*, 7565.
- (29) Ravel, B.; Newville, M. *J. Synchrotron Radiat.* **2005**, *12*, 537.
- (30) Newville, M. *J. Synchrotron Radiat.* **2001**, *8*, 322.
- (31) Ravel, B. *J. Synchrotron Radiat.* **2001**, *8*, 314.
- (32) Zabinsky, S. I.; Rehr, J. J.; Ankudinov, A.; Albers, R. C.; Eller, M. *J. Phys. Rev. B* **1995**, *52*, 2995.
- (33) Rehr, J. J.; Albers, R. C. *Phys. Rev. B* **1990**, *41*, 8139.
- (34) Jayaram, V.; Rajkumar, J.; Rani, B. S. *J. Am. Ceram. Soc.* **1999**, *82*, 473.
- (35) Schaedler, T. A.; Gandhi, A. S.; Saito, M.; Rühle, M.; Gambino, R.; Levi, C. G. *J. Mater. Res.* **2006**, *12*, 791.
- (36) Straumal, B. B.; Mazilkin, A. A.; Protasova, S. G.; Myatev, A. A.; Straumal, P. B.; Baretzky, B. *Acta Mater.* **2008**, *56*, 6246.
- (37) Straumal, B.; Baretzky, B.; Mazilkin, A.; Protasova, S.; Myatev, A.; Straumal, P. *J. Eur. Ceram. Soc.* **2009**, *29*, 1963.
- (38) Brehm, J. U.; Winterer, M.; Hahn, H. *J. Appl. Phys.* **2006**, *100*, 064311.
- (39) Hinds, W. C. Physical and Chemical Changes in the Particulate Phase. In *Aerosol Measurement*; Baron, P. A., Willeke, K., Eds.; John Wiley & Sons: New York, 2001; p 83.
- (40) Shannon, R. D. *Acta Crystallogr., Sect. A* **1976**, *32*, 751.
- (41) Jin, Z.; Fukumura, T.; Kawasaki, M.; Ando, K.; Saito, H.; Sekiguchi, T.; Yoo, Y. Z.; Murakami, M.; Matsumoto, Y.; Hasegawa, T.; Koinuma, H. *Appl. Phys. Lett.* **2001**, *78*, 3824.
- (42) Woltersdorf, J.; Nepijko, A. S.; Pippel, E. *Surf. Sci.* **1981**, *106*, 64.
- (43) Combe, N.; Chassaing, P. M.; Demangeot, F. *Phys. Rev. B* **2009**, *79*, 045408.
- (44) Kim, M.; Hong, Y. J.; Yoo, J.; Yi, G.-C.; Park, G.-S.; Kong, K.-J.; Chang, H. *Phys. Stat. Sol.* **2008**, *2*, 197.
- (45) Desgreniers, S. *Phys. Rev. B* **1998**, *58*, 14102.
- (46) Kisi, E. H.; Elcombe, M. M. *Acta Crystallogr.* **1989**, *C45*, 1867.
- (47) Zhang, Y. H.; Assadi, M. H. N.; Li, S. *J. Phys.: Condens. Matter.* **2009**, *21*, 175802.
- (48) Zhang, Y. B.; Sritharan, T.; Li, S. *Phys. Rev. B* **2006**, *73*, 172404.
- (49) Toulemonde, O.; Gaudon, M. *J. Phys. D: Appl. Phys.* **2010**, *43*, 045001.
- (50) Li, J.-J.; Hao, W.-C.; Xu, H.-Z.; Wang, T.-M. *J. Appl. Phys.* **2009**, *105*, 053907.